

# Multi-scale Sampling and Aggregation Network For High Dynamic Range Imaging

Jun Xiao, Qian Ye, Tianshan Liu, Cong Zhang, Kin-Man Lam

**Abstract**—High dynamic range (HDR) imaging is a fundamental problem in image processing, which aims to generate well-exposed images, even in the presence of varying illumination in the scenes. In recent years, multi-exposure fusion methods have achieved remarkable results, which merge multiple low dynamic range (LDR) images, captured with different exposures, to generate corresponding HDR images. However, synthesizing HDR images in dynamic scenes is still challenging and in high demand. There are two challenges in producing HDR images: 1). Object motion between LDR images can easily cause undesirable ghosting artifacts in the generated results. 2). Under and overexposed regions often contain distorted image content, because of insufficient compensation for these regions in the merging stage. In this paper, we propose a multi-scale sampling and aggregation network for HDR imaging in dynamic scenes. To effectively alleviate the problems caused by small and large motions, our method implicitly aligns LDR images by sampling and aggregating high-correspondence features in a coarse-to-fine manner. Furthermore, we propose a densely connected network based on discrete wavelet transform for performance improvement, which decomposes the input into several non-overlapping frequency subbands and adaptively performs compensation in the wavelet domain. Experiments show that our proposed method can achieve state-of-the-art performances under diverse scenes, compared to other promising HDR imaging methods. In addition, the HDR images generated by our method contain cleaner and more detailed content, with fewer distortions, leading to better visual quality.

**Index Terms**—High Dynamic Range Imaging, Image Enhancement, Image Restoration

## I. INTRODUCTION

High dynamic range (HDR) imaging is a fundamental problem in image processing and computational photography, which aims to generate high-quality and well-exposed images, even in varying lighting conditions. Most modern imaging systems, such as digital cameras, often fail to capture the full range of natural lighting, because of inherent hardware limitations. Therefore, HDR imaging is a dispensable technique in modern imaging systems and has high industrial values.

At the early stage, researchers in [1, 2] attempted to design specific hardware devices for generating high-quality HDR images, but these devices were too expensive to be widely used in commercial products. Alternatively, many researchers focus on the multi-exposure fusion approach, which takes a sequence of low dynamic range (LDR) images with different exposures

and merges them to generate the corresponding HDR images based on a reference LDR image. However, most multi-exposure fusion methods fail to produce satisfactory results from LDR images captured in dynamic scenes [3]. Unlike static scenes, dynamic scenes introduce two challenging issues for HDR imaging. The first one is that intensive motion between LDR images is prone to producing ghosting artifacts and significantly reduce the quality of the generated HDR images. Besides that, the corrupted content in under and overexposed regions will lead to undesirable distortions, if they are not adequately compensated in the merging stage.

In recent years, motion-removal-based methods [4–13] and alignment-based methods [6, 14–17] have shown their effectiveness for HDR imaging in dynamic scenes. For motion-removal-based methods, motion regions are first detected, and then removed in the merging stage. Therefore, object motions are not considered in the reconstruction, and ghosting artifacts are reduced in the generated results. To accurately detect motion regions, various methods have been proposed, including threshold-based methods [5, 6, 8, 9], gradient-based methods [18, 19], and low-rank and sparsity-based methods [10–12]. However, these motion-removal-based methods suffer from two intrinsic limitations. Firstly, ghosting artifacts are easily introduced, because of inaccurate motion detection, which seriously degrades the quality of generated HDR images. In addition, when the input LDR images contain large-scale motions, a large amount of pixels are removed in the merging processing, which inevitably causes information loss and harms the performance. A recent work [13] proposed a deep learning-based model with the spatial attention mechanism to avoid information loss in moving regions. The unnecessary pixels are suppressed in a soft manner before the merging stage. However, ghosting artifacts still appear in the generated images, as shown in [3].

Unlike motion-removal-based methods, alignment-based methods first align the input LDR images with a reference from the input, and then merge them to generate the corresponding HDR images. For example, Kalantari *et al.* [15] used optical flow [20] to align the input LDR images and then, adopted a deep convolutional neural network (CNN) to merge the aligned LDR images for reconstruction. However, the illumination in LDR images may vary significantly, so the brightness constancy condition required by optical flow is hard to satisfy [21–23] and the resulting optical flow is inaccurate, which further harms the quality of the generated HDR images. Instead of using optical flow, Wu *et al.* [17] adopted a homography transformation to globally register LDR images in the pre-processing stage. Then, a deep CNN

Jun Xiao, Tianshan Liu, Cong Zhang and Kin-Man Lam are with the Department of Electronic and Information Engineering, the Hong Kong Polytechnic University. E-mail: jun.xiao@connect.polyu.hk

Qian Ye is with Graduate School of Information Sciences, Tohoku University. E-mail: qian@vision.is.tohoku.ac.jp

Manuscript received July 30, 2022;

model with the U-Net shape structure is used to extract multi-scale features for reconstruction. However, this method does not consider local information and thus cannot effectively compensate for corrupted image content in saturated regions. Inspired by the deformable convolution [24], Pu *et al.* [25] adopted a pyramid, cascading and deformable (PCD) alignment module [26] to hierarchically align LDR images for reconstruction. Furthermore, Liu *et al.* [27] proposed a dual-branch network for HDR imaging in dynamic scenes, which adopts the spatial attention mechanism and the PCD module in different branches, respectively. However, deformable convolution suffers from unstable training [28]. In addition, the receptive field of deformable convolution is restricted by its kernel size, making it difficult to handle large-scale motions.

In this paper, we propose a multi-scale sampling and aggregation network for HDR imaging in dynamic scenes. Unlike previous methods, our method performs intra-scale aggregation and inter-scale aggregation to implicitly align LDR images in a coarse-to-fine manner. Specifically, in each scale space, intra-scale aggregation samples neighboring features around misaligned pixels and aggregates sampled features according to their correspondences with the reference features. These features are of higher quality because they are more similar to the corresponding reference features. Thus, the high-quality correspondence features can contribute more to aggregation for alignment. Furthermore, inter-scale aggregation progressively fuses the aggregated features across different scale spaces. Therefore, ghosting artifacts, caused by small and large motions in LDR images, are effectively reduced. In addition, a densely connected network based on discrete wavelet transform is proposed for performance improvement. The proposed dense wavelet network decomposes the input features into several non-overlapping frequency subbands and compensates for the image content in the wavelet domain. As shown in Fig. 1, different frequency subbands can provide different information for reconstruction. For example, the low-frequency subband mainly contains coarse image content, while the high-frequency subbands have rich structural information, which is beneficial for HDR imaging. The main contributions of this paper are summarized as follows:

- 1) We propose a multi-scale sampling and aggregation network for HDR imaging in dynamic scenes. In this method, intra-scale and inter-scale aggregation schemes are proposed to implicitly align LDR images from coarse-to-finer scales.
- 2) We further propose a densely connected network, based on discrete wavelet transform for performance improvement, which can effectively compensate for corrupted content in saturated regions.
- 3) Experiments show that our proposed method significantly outperforms other promising HDR imaging methods and generates remarkable results. In addition, the HDR images generated by our method have more structural information and fewer distortions, leading to better and higher visual quality.

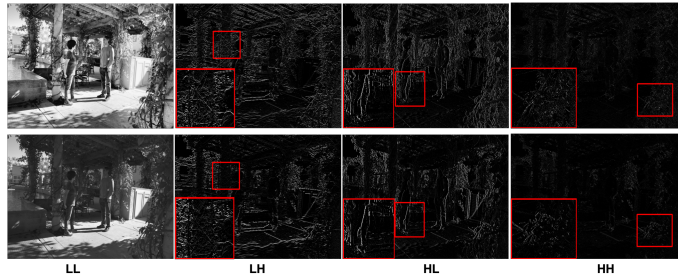


Fig. 1. Illustration of an HDR image (the first row) and the corresponding LDR image (the second row) in the wavelet domain. LL, LH, HL, and HH represent the low-low band, low-high band, high-low band, and high-low band, respectively. The region marked by a red box in an image is enlarged and placed at the bottom-left corner.

## II. RELATED WORKS

### A. Motion Removal-based Methods

Motion detection is a key point in motion removal-based methods. Bogoni [4] applied a non-parametric model to detect under and overexposed regions before merging LDR images. In [9], misaligned regions are rejected according to the error map of aligned pixels. Khan *et al.* [5] proposed an method to detect moving regions implicitly and iteratively fuses the LDR images, so undesirable artifacts were reduced. Jacobs *et al.* [6] assumed that moving objects cause large variations of pixel intensity in overexposed regions. Based on this assumption, they proposed a motion-detection method based on measuring variance [7]. Gallo *et al.* [8] assumed that irradiance values of the background are linear to the exposure time, and proposed a method for detecting ghosting regions based on the irradiance deviation. All these methods utilize local information in regular patch grids. Instead, Raman and Chaudhui [29] proposed to group pixels in images into superpixels and a bottom-up framework to detect the ghosting regions. This method can effectively handle irregular objects in saturated regions. Heo *et al.* [30] proposed a coarse-to-fine pipeline to detect motion regions, which first applies a joint probability model to different images to roughly detect motion regions and then refines these regions with graph cut. Rather than detecting motion regions in the spatial domain, Zhang and Cham [18] proposed a motion-detection method based on the assumption that gradient values change significantly in motion regions. However, this method struggles to obtain gradient information for saturated regions, which inevitably harms the performance. Lee *et al.* [12] formulated the motion-detection problem as a rank-minimization problem, which considers misalignment errors, moving objects, noise, and nonlinear artifacts as sparse outliers. Oh *et al.* [10] further extended the low-rank model in [12] by introducing user control for moving objects under different exposure settings, which obtained better results. Yan *et al.* [11] considered that moving objects in LDR images have the sparsity property, and thus a regularized sparsity-based model was proposed for motion detection. Yan *et al.* [13] proposed a deep CNN-based model, where the spatial attention mechanism is used to suppress misaligned regions at the feature level. However, motion removal-based methods have several inherent limitations. 1). When there are large-scale

motions between the LDR images, a large amount of pixels are excluded in the merging process, resulting in distorted content. 2). The quality of the generated HDR images is very sensitive to detection accuracy and is not robust to varying illumination.

### B. Alignment-based Methods

Alignment-based methods can be divided into three categories: flow-based methods, deformable-based methods, and patch-based methods. Flow-based methods mainly adopt optical flow and its variants to align LDR images and then merge the aligned LDR images to generate the corresponding HDR images. Tomaszewska and Mantiuk [31] used a homography transform to globally register LDR images before merging. The registered LDR images are fused for HDR imaging by the radiometric calibration method [32]. As illumination varies significantly in LDR images, the brightness constancy condition is easily violated in the spatial domain. Zimmer *et al.* [33] proposed to estimate optical flow in the gradient domain, which guarantees the consistency of gradients. However, this method treats flow estimation and HDR image generation separately, which may lead to sub-optimal performance. Hafner *et al.* [16] proposed a method for jointly estimating optical flow and reconstructing HDR images, so the performance is further improved. By considering corrupted contents in saturated regions, Hu *et al.* [34] proposed a method to merge LDR images in the luminance domain, effectively reducing the intervention in saturated regions. Inspired by the unprecedented success achieved by deep learning models in many vision tasks, Kalantari and Ramamoorthi [15] proposed a deep learning-based network for HDR imaging, called DeepHDR. Their method first aligns the LDR images using the optical flow [20] and then forwards the aligned LDR images to a deep CNN network for fusion. Unlike the method [35] using dense motion fields, Wu *et al.* [17] propose a deep translation-based method that globally registers LDR images with a homography function and then extracts multi-scale features for reconstruction. However, flow-based methods rely on the accuracy of optical-flow estimation and are very sensitive to varying illumination, so these methods are prone to generating undesirable ghosting artifacts in the generated HDR images. Inspired by deformable convolution [24], many researchers have paid attention to deep deformable-based methods for HDR imaging. For example, Pu *et al.* [25] proposed to progressively align LDR images and reconstruct HDR images with the PCD module [26] and achieved promising results. Liu *et al.* [27] further improved the method [25] by introducing a dual-branch structure which is composed of the PCD module and the spatial attention mechanism. The output of each branch contains different features of the LDR images, so the performance can be improved. However, deformable-based methods cannot effectively handle large-scale motions, because the receptive field of the deformable convolutions is restricted by its kernel size. In addition, deformable convolution suffers from unstable training [28]. Instead of explicit alignment using optical flow or deformable convolution, Sen *et al.* [36] proposed a patch-based method to reconstruct HDR images, which uses a patch-match algorithm to find similar patches

for reconstruction. Yan *et al.* [37] used the non-local attention mechanism in a deep CNN model, which captures pixel-wise correspondence for reconstruction. Chen *et al.* [38] proposed a hybrid method for HDR imaging, which first reduces the effect caused by motions with the spatial attention mechanism and then aggregates the most similar patch in a coarse-to-finer manner. Patch-based methods implicitly align LDR images, but these methods are too computationally expensive. Motivated by RAFT [23], Ye *et al.* [3] proposed to progressively select features from intermediate layers to reconstruct HDR images, which implicitly aligns LDR images in the feature space. To compensate for the missing content in under and overexposed regions, Niu *et al.* [39] proposed a generative adversarial network (GAN)-based model, but GAN models suffer from model collapse and unstable training [40–42], so this method is prone to artifacts and harms the performance.

Compared with flow-based methods and deformable-based methods, our proposed method has several advantages: 1). Flow-based methods use optical flow to globally sample one position for alignment, but our proposed method samples multiple neighboring positions around the misaligned pixels for alignment in a coarse-to-fine manner. 2). Our proposed method adaptively aggregates the sampled features which are more similar to the reference features, so ghosting artifacts can be effectively reduced. 3). The number of sampled features in our proposed method is not limited by the kernel size, which provides greater flexibility than deformable-based methods.

## III. THE PROPOSED METHODS

In this paper, we propose a multi-scale sampling and aggregation network for HDR imaging in dynamic scenes. As shown in Fig. 2, the proposed model consists of two important sub-networks, i.e., the multi-scale correspondence alignment sub-network and the dense wavelet sub-network, for alignment and reconstruction, respectively. In this section, we will first describe the pre-processing stage and the multi-scale correspondence alignment sub-network that includes the encoder and the multi-scale sampling and aggregation module (Multi-scale SAM). Then, we will introduce the proposed dense wavelet sub-network. Finally, the loss function used to train our model will be described in detail.

### A. The Pre-processing Stage

Given a sequence of LDR images  $\{I_L^{(1)}, I_L^{(2)}, \dots, I_L^{(N)}\}$  with  $N$  different exposure times, the target of HDR imaging is to reconstruct a clean and ghost-free HDR image  $I_H^{(r)}$ , which is aligned with the reference image  $I_L^{(r)}$ , where  $r \in \{1, 2, \dots, N\}$ . Without loss of generality, we consider three LDR images with low, medium, and high exposure conditions in our method, denoted as  $\{I_L^{(1)}, I_L^{(2)}, I_L^{(3)}\}$ , and take the LDR image  $I_L^{(2)}$ , which is captured with medium exposure time, as the reference. Since HDR imaging involves manipulation of illumination values, we first linearize the input LDR images with gamma correction. The linearized LDR images are computed as follows:

$$\hat{I}_L^{(i)} = \frac{(I_L^{(i)})^\gamma}{t_i}, \quad i = 1, 2, 3, \quad (1)$$

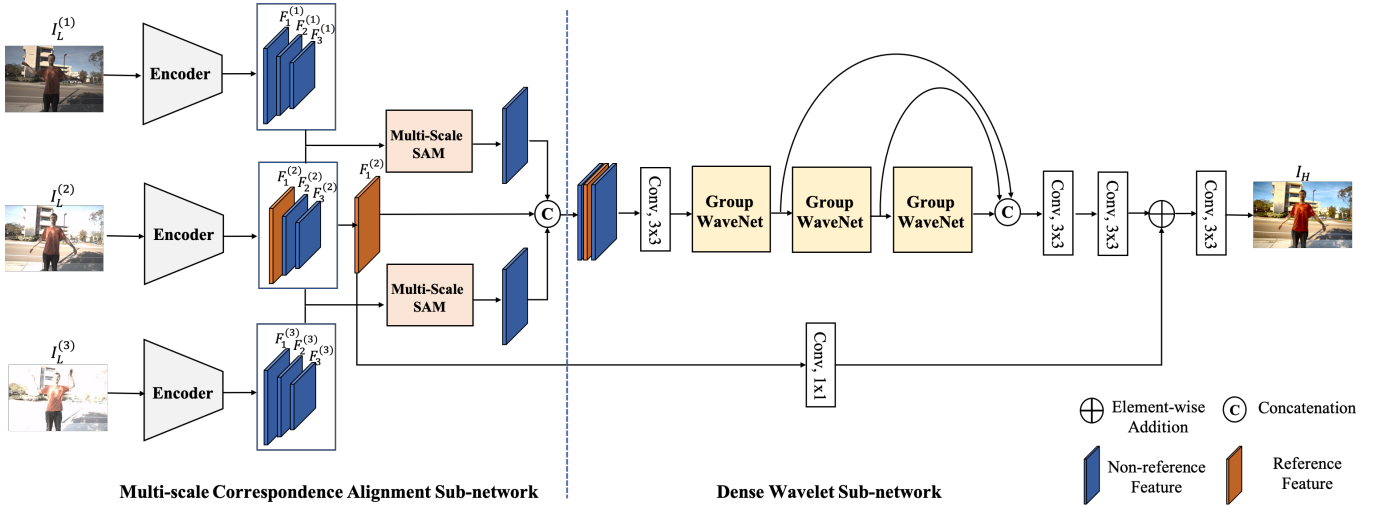


Fig. 2. The overall structure of the proposed multi-scale sampling and aggregation network, which consists of a multi-scale correspondence alignment sub-network and a dense wavelet sub-network.  $F_j^{(i)}$  denotes the features extracted from  $X_i$  in the  $j$ -th scale space, where  $i, j = 1, 2, 3$ .

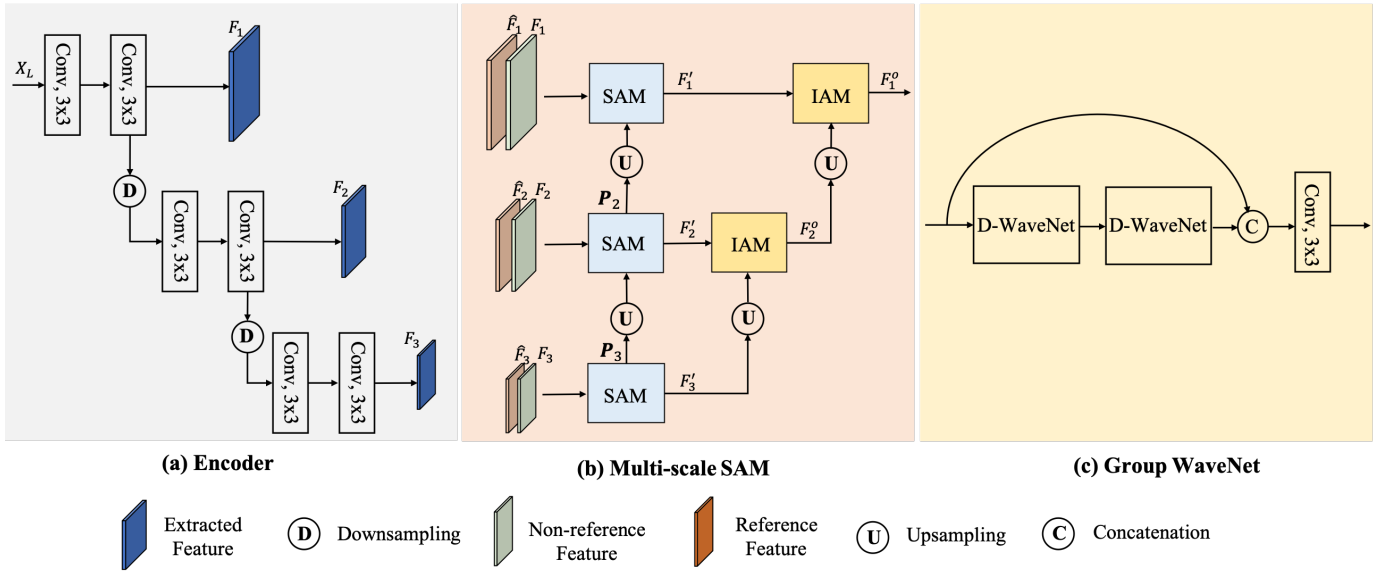


Fig. 3. The overall structure of the encoder, multi-scale SAM, and Group WaveNet, respectively. In Encoder,  $X_L$  denotes the input 6-channel tensor and  $F_i$  represents the extracted features of different scales, for  $i = 1, 2, 3$ . In (b),  $\hat{F}_i$  and  $F_i$  denote the reference and non-reference features, respectively, where  $i = 1, 2, 3$ .

where  $\hat{I}_L^{(i)}$  is the linearized image of the  $i$ -th input LDR image  $I_L^{(i)}$ ,  $\gamma > 1$  is a hyper-parameter for gamma correction, and  $t_i$  denotes the exposure time of the LDR image  $I_L^{(i)}$ . In our method, we follow the suggestions in [15] and empirically set  $\gamma$  to 2.2. Then, the LDR images  $I_L^{(i)}$  and their corresponding linearized images  $\hat{I}_L^{(i)}$  are concatenated to form a 6-channel tensor  $X_i = [I_L^{(i)}, \hat{I}_L^{(i)}]$ , for  $i = 1, 2, 3$ , which is the input of our proposed model.

Given a number of HDR-LDR image pairs, our model attempts to learn a highly nonlinear illumination mapping from the LDR domain to the HDR domain. The estimated HDR image  $\hat{I}_H$  is generated as follows:

$$\hat{I}_H = f_\theta(X_1, X_2, X_3), \quad (2)$$

where  $f_\theta(\cdot)$  denotes the proposed model with parameters  $\theta$ .

### B. The Multi-scale Correspondence Alignment Sub-network

The multi-scale correspondence alignment sub-network aims to implicitly align the input LDR images in a coarse-to-finer manner, which consists of two key components, namely the encoder and multi-scale sampling aggregation module (Multi-scale SAM). The overall structure of the multi-scale correspondence alignment sub-network is shown in Fig. 2.

1) *Encoder*: The encoder takes  $\{X_1, X_2, X_3\}$  as input and extracts corresponding multi-scale features. As shown in Fig. 3, the encoder in our method contains three scale spaces. In each scale space, two convolutional layers with a kernel size of  $3 \times 3$  are used to generate features. The



downsampling operator is a convolutional layer with a stride of 2. In our method, the kernel weights of the encoders are shared among the three inputs, so the required computational complexity and model complexity are reduced. The generated multi-scale features are denoted as  $\mathbf{F}_i = \{F_i^{(1)}, \dots, F_i^{(S)}\}$ , for  $i = 1, 2, 3$ , where  $S$  is the number of scales. Then, these multi-scale features are forwarded to multi-scale SAM modules for progressive alignment in a coarse-to-fine manner.

2) *Multi-Scale Sampling Aggregation Module (Multi-scale SAM)*: As illustrated in Fig. 3(b), the Multi-scale SAM module contains two important parts, namely the sampling aggregation module (SAM) and the inter-scale aggregation module (IAM).

**Sampling and Aggregation Module (SAM)**. For each scale space, SAM aligns pixels in the non-reference features by sampling its neighboring features and then adaptively aggregating sampled features according to their correspondence with the reference features. As illustrated in Fig. 4, the proposed SAM module consists of three parts: sample generator, correspondence computation, and sample aggregation. Given two input features at the  $s$ -th scale space, denoted as  $F_s$  and  $\hat{F}_s$ , which are the features extracted from the non-reference image and the reference image, respectively, the sample generator takes these two features, as well as the sampling map  $P_{s-1}$  from the previous scale space as input and generates the sampling map of the  $s$ -th scale space  $P_s$ . The sampling map  $P_{s-1}$  contains the coarse sampling information of the  $(s-1)$ -th scale space, so it can be used as the prior information to guide the generation of the sampling map of the  $s$ -th scale space. In our method, the sample generator is a small convolutional network with four convolutional layers, and the sampling map  $P_s$  is computed as follows:

$$P_s = g(F_s, \hat{F}_s, \hat{P}_{s-1}), \quad (3)$$

where  $g(\cdot)$  denotes the sampling generator and  $P_s = [p_s^{(1)}, \dots, p_s^{(N)}]$  represents the  $N$  sampling matrices for the  $s$ -th scale space, where the sampling matrix  $p_s^{(i)}$  is  $H \times W \times 2$  dimensional, for  $i = 1, \dots, N$ .  $H$  and  $W$  represent the height and width of the input features, respectively. These sampling matrices provide the locations of corresponding sampled features for each pixel position. Specifically, for the  $s$ -th scale space, the element of the  $i$ -th sampling matrix at the position  $(m, n)$  is a two-dimensional vector, denoted as  $p_{s,m,n}^{(i)} = [p_{s,m,n}^{(i)}(x), p_{s,m,n}^{(i)}(y)]$ . This vector contains the displacement information in the horizontal and vertical directions between the sampled feature and the reference feature. Based on the sampling matrices, the sampled features of the pixel position  $(m, n)$  are computed as follows:

$$\bar{F}_s^{(i)}(m, n) = F_s(m + p_{s,m,n}^{(i)}(x), n + p_{s,m,n}^{(i)}(y)), \quad (4)$$

where  $\bar{F}_s^{(i)}(m, n)$  denotes the  $i$ -th sampled feature corresponding to the misaligned pixel at the position  $(m, n)$  of the  $s$ -th scale space, for  $i = 1, \dots, N$ . For fractional positions (i.e.,  $m + p_{s,m,n}^{(i)}(x) \notin \mathbb{Z}$  or  $n + p_{s,m,n}^{(i)}(y) \notin \mathbb{Z}$ ), bilinear interpolation is used to compute the values. In the  $s$ -th scale space, SAM samples neighboring features for all misaligned pixels according to the location information provided by the sampling map  $P_s$ . However, not all the sampled features are

beneficial for reconstructing HDR images, especially in saturated regions. Therefore, we propose a method to adaptively aggregate the sampled features. In particular, we first calculate the correspondence between the sampled features and the reference features at each pixel position, which are based on the dot product between the sampled features and the reference features. The sampled features having higher correspondence means that they are more similar to the reference features, while the sampled features with lower correspondences are less similar to the reference features. Then, we compute the correspondence weights for aggregation. For the position  $(m, n)$ , the weight is computed as follows:

$$w_{m,n}^{(i)} = \frac{\exp(\bar{F}_s^{(i)}(m, n) \cdot \hat{F}_s(m, n))}{\sum_{j=1}^N \exp(\bar{F}_s^{(j)}(m, n) \cdot \hat{F}_s(m, n))}, \quad (5)$$

where  $\cdot$  denotes the dot product and  $0 \leq w_{m,n}^{(i)} \leq 1$ , for  $i = 1, \dots, N$ . Next, the non-reference features are aligned by aggregating the sampled features according to the computed weights, and the corresponding aligned feature  $\hat{F}_s(m, n)$  is computed as follows:

$$\hat{F}_s(m, n) = w_{m,n}^{(1)} \bar{F}_s^{(1)}(m, n) + \dots + w_{m,n}^{(N)} \bar{F}_s^{(N)}(m, n). \quad (6)$$

As observed, aligned features are generated by a linear combination of the sampled features. For those sampled features having high correspondence with the reference feature, the corresponding weights will be larger, so these features will have more contribution to the aggregation. For those sampled features with lower correspondence, the associated weights will be smaller. This can effectively alleviate undesirable effects caused by dissimilar features in aggregation and avoid ghosting artifacts.

**Inter-scale Aggregation Module (IAM)**. The input LDR images are captured in dynamic scenes, so they unavoidably contain small and large-scale motions. To address this issue, we propose the inter-scale aggregation module to progressively aggregate the output features of different scales. The overall structure of IAM is shown in Fig. 5. Given two output features  $\hat{F}_s$  and  $\hat{F}_{s-1}'$  from the  $s$ -th and  $(s-1)$ -st scales, the average pooling and the max pooling are applied to these two features to extract local features. Then, the local features are concatenated along the channel dimension. A convolutional layer is applied to the concatenated features to generate a fusion mask  $M$ . Each element of the fusion mask  $M$  is in  $[0, 1]$ . The two input features from adjacent scales are adaptively aggregated based on this fusion mask to produce the corresponding output features  $F_s^{(\text{out})}$ , which are computed as follows:

$$F_s^{(\text{out})} = (1 - M) \odot F_s + M \odot F_{s-1}', \quad (7)$$

where  $\odot$  denotes the Hadamard product. The two input features are spatially fused by linear combination based on the computed fusion mask  $M$ . The coarse-scale features contain more contextual information, while the finer-scale features have more detailed information. The fusion mask performs feature selection between the two input features from adjacent scales in a soft manner. Benefiting from this multi-scale structure, small and large-scale motions in LDR images are aligned in a coarse-to-finer manner.

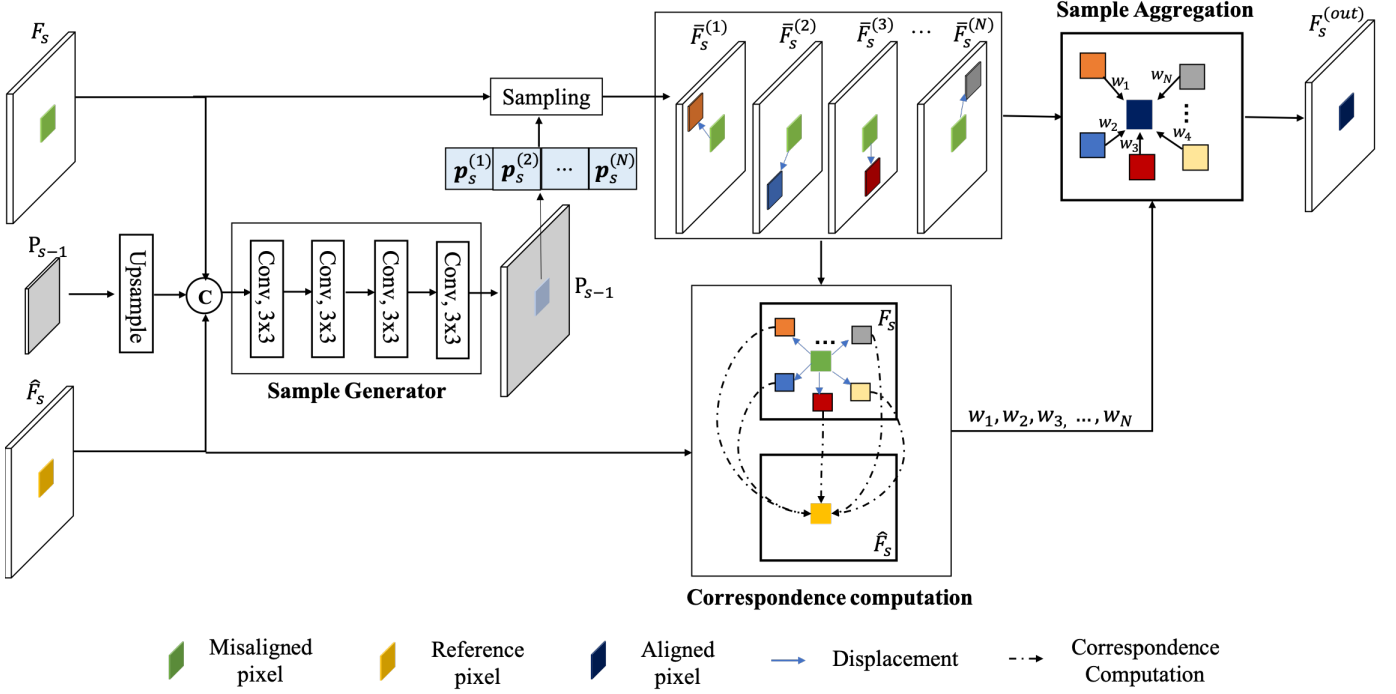


Fig. 4. The overall structure of the sampling and aggregation module (SAM).  $F_s$  and  $\hat{F}_s$  denote the non-reference and reference features of the  $s$ -th scale space.  $P_s$  and  $P_s$  are the sets containing sampling positions.  $p_s^{(i)}$  denotes the  $i$ -th sampling position in the  $s$ -th scale space, where  $i = 1, \dots, N$  and  $N$  is the number of samples.  $\bar{F}_s^{(i)}$  denotes the  $i$ -th sample feature in the  $s$ -th scale space.  $\{w_1, \dots, w_N\}$  are  $N$  aggregation weights.  $F_s^{(out)}$  is the output feature associated with  $F_s$ .

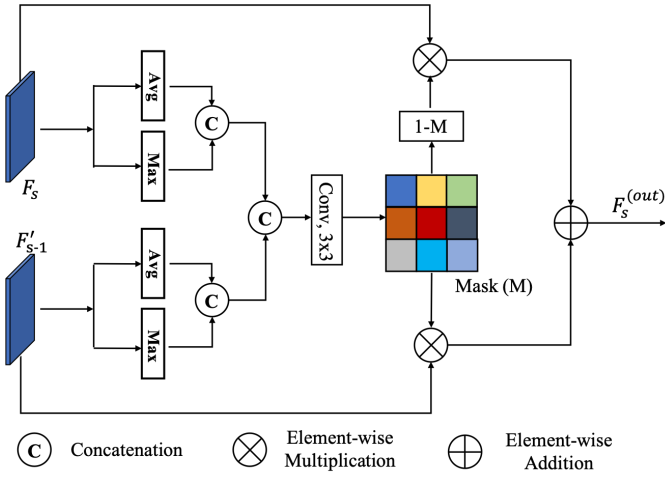


Fig. 5. The overall structure of the inter-scale aggregation module.  $F_s$  and  $F_{s-1}'$  denote the input from the  $s$ -th and  $(s-1)$ -th scale spaces, respectively. ‘‘Avg’’ and ‘‘Max’’ stand for average pooling and max pooling, respectively.  $F_s^{(out)}$  is the output feature of the  $s$ -th scale space.

### C. Dense Wavelet Sub-network

1) *Network Structure*: As illustrated in Fig. 2, the dense wavelet sub-network is responsible for merging aligned features and generating corresponding HDR images. Specifically, the dense wavelet sub-network first concatenates the aligned features (i.e.,  $F_1^{1 \rightarrow 2}$  and  $F_1^{3 \rightarrow 2}$ ) and the reference feature  $F_1^2$  along the channel dimension, where  $F_1^{i \rightarrow 2}$  denotes the features generated by aligning  $F_1^i$  with the reference feature

$F_1^2$ , where  $i = 1$  or  $3$ . Then, a convolutional layer with a kernel size of  $3 \times 3$  is applied to compress and fuse the concatenated features. The resulting fused feature is forwarded to three group-wavelet modules (Group WaveNets) for feature extraction in the wavelet domain. Each Group WaveNet is composed of two small, cascaded Dense wavelet networks (D-WaveNets), as shown in Fig. 3(c), which play a significant role in feature extraction and HDR image reconstruction. In our method, the output of the second D-WaveNet is concatenated with the input, followed by a convolutional layer for feature fusion. Furthermore, the outputs of the three Group WaveNets are concatenated, followed by two convolutional layers for fusion. Therefore, the proposed dense wavelet sub-network has a structure with the local-global dense connections. This can significantly increase the information interaction and fully utilize the features from different layers. At the output of the network, the estimated HDR  $\hat{I}_H$  images are computed as follows:

$$\hat{I}_H = F' + \text{Conv}(F_1^2), \quad (8)$$

where  $F'$  denotes the fused feature generated by the two convolutional layers and  $\text{Conv}(\cdot)$  represents the convolutional layer with a kernel size of one.

2) *Dense Wavelet Network (D-WaveNet)*: The D-WaveNet, based on discrete wavelet transform (DWT), decomposes input features into several non-overlapping frequency subbands for feature extraction. The overall structure of D-WaveNet is illustrated in Fig. 6. Given an input feature map denoted as  $F$ , DWT is applied to  $F$  along the channel dimension, and then four frequency subbands are obtained, i.e., one low-

frequency subband and three high-frequency subbands. These four frequency subbands are computed as follows:

$$W_{LL} = \mathcal{L}F\mathcal{L}^T, W_{LH} = \mathcal{H}F\mathcal{L}^T \quad (9)$$

$$W_{HL} = \mathcal{L}F\mathcal{H}^T, W_{HH} = \mathcal{H}F\mathcal{H}^T \quad (10)$$

where  $W_{LL}$  denotes the low-frequency subband and  $\{W_{LH}, W_{HL}, W_{HH}\}$  represent the high-frequency sub-bands in the horizontal, vertical, and diagonal directions, respectively.  $\mathcal{L}$  denotes the matrix containing all the low-frequency filters  $\{\ell_i\}_{i \in \mathbb{Z}}$  and  $\mathcal{H}$  is the matrix containing all the high-frequency filters  $\{h_i\}_{i \in \mathbb{Z}}$  for decomposition, where

$$\mathcal{L} = \begin{pmatrix} \cdots & \cdots & \cdots & & & & \\ \cdots & \ell_{-1} & \ell_0 & \ell_1 & \cdots & \cdots & \\ & & \cdots & \ell_{-1} & \ell_0 & \ell_1 & \cdots \\ & & & & \cdots & \cdots & \cdots \end{pmatrix}, \quad (11)$$

and

$$\mathcal{H} = \begin{pmatrix} \cdots & \cdots & \cdots & & & & \\ \cdots & h_{-1} & h_0 & h_1 & \cdots & \cdots & \\ & & \cdots & h_{-1} & h_0 & h_1 & \cdots \\ & & & & \cdots & \cdots & \cdots \end{pmatrix}. \quad (12)$$

In our method, Haar wavelets are adopted for feature decomposition, because Haar wavelets have orthogonal and biorthogonal properties. These two properties guarantee that the input features can be perfectly reconstructed without concerns about introducing distortions. After decomposition, all frequency subbands are concatenated along the channel dimension and forwarded to three dilated convolutional layers with dense connections for feature extraction over the wavelet domain. The dilated rate of these three convolutional layers are set to 1, 2, and 3, respectively, in our method.

At the output of D-WaveNet, the extracted features are transferred from the wavelet domain to the spatial domain with the inverse DWT (IDWT), which is computed as follows:

$$\hat{F} = \mathcal{L}^T \hat{W}_{LL} \mathcal{L} + \mathcal{H}^T \hat{W}_{LH} \mathcal{L} + \mathcal{L}^T \hat{W}_{HL} \mathcal{H} + \mathcal{H}^T \hat{W}_{HH} \mathcal{H}, \quad (13)$$

where  $\{\hat{W}_{LL}, \hat{W}_{LH}, \hat{W}_{HL}, \hat{W}_{HH}\}$  denote four output wavelet subbands, and  $\hat{F}$  is the corresponding output feature in the spatial domain. Then, we use a residual connection and the channel attention mechanism [43] to generate the output feature  $F_{\text{out}}$  as follows:

$$F_{\text{out}} = \text{CA}(\hat{F}) + F, \quad (14)$$

where  $\text{CA}(\cdot)$  is the channel attention mechanism, which scales the features along the channel dimension.

#### D. Loss Function

Since HDR images are usually displayed on the screen after tone mapping, we calculate the loss in tone-mapped images. Although many effective tone-mapping methods were proposed in the past decades, they are not differentiable and cannot be used as a loss function for training deep neural

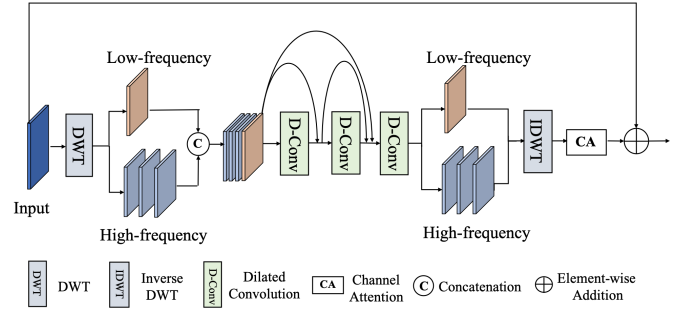


Fig. 6. The overall structure of D-WaveNet. The dilated rates of the three dilated convolutional layers are set to 1, 2, and 3, respectively.

networks. In our method, we apply the  $\mu$ -law function to compress the output of our network, because the  $\mu$ -law function is a widely used range compressor in audio processing and is differentiable. Specifically, given an image  $I$  in the linear domain, the corresponding tone-mapped image is computed as follows:

$$T(I) = \frac{\log(1 + \mu I)}{\log(1 + \mu)}, \quad (15)$$

where  $\mu$  denotes a hyper-parameter defining the extent of compression and is set to 5000 in our method. We use the  $L_1$  norm to compute the distance between the output  $\hat{I}_H$  and the ground-truth image  $I_H$  after tone mapping. Formally, the loss function is defined as follows:

$$L(\hat{I}_H, I_H) = \|T(\hat{I}_H) - T(I_H)\|_1. \quad (16)$$

In our method, the range of the output is restricted to  $[0, 1]$  by using the sigmoid function.

## IV. EXPERIMENTS AND ANALYSIS

### A. Experiment Settings

1) *Datasets*: In the experiments, a public dataset [15], called the Kalantari dataset, was used to train our model, which has a total of 90 samples. Each sample contains three LDR images and a ground-truth HDR image, with exposure basis of  $\{-2, 0, +2\}$  or  $\{-3, 0, +3\}$ . All images in this dataset are captured in static and dynamic scenes. Following previous works [11, 15, 17, 38], we used 75 samples for training and 15 samples for testing. Besides that, we additionally adopted two challenging datasets, namely the Sen dataset [36] and the Tursun dataset [44], to evaluate the generalization of the proposed model. However, these two datasets do not provide ground-truth images for quantitative comparison.

2) *Evaluation metrics*: HDR images are displayed on screens through tone mapping, so we evaluate the peak signal-to-noise ratio (PSNR) and the structural similarity index measure (SSIM) on the tone-mapped images, which are denoted as PSNR- $\mu$  and SSIM- $\mu$ , respectively. For the sake of completeness, we also include the PSNR and SSIM results of the generated images in the linear domain, denoted as PSNR-L and SSIM-L, respectively. Furthermore, we adopted the HDR-VDP-2 metric in the evaluation. This metric is specifically designed to assess the quality of HDR images [45]. If the generated HDR images have higher HDR-VDP-2 score, the quality of the generated HDR images is better.

3) *Implementation details*: Due to the large size of the training images, we divided the input images into image patches of the size  $200 \times 200$  pixels for training, for training. All training samples are randomly flipped vertically or horizontally, and rotated by  $90^\circ$ ,  $180^\circ$  or  $270^\circ$  for data augmentation. We adopted the AdamW algorithm, with  $\beta_1 = 0.9$  and  $\beta_2 = 0.999$ , to adaptively update the parameters of the proposed model. In the training stage, the batch size is set to 16 and the initial learning rate is set to  $2.0 \times 10^{-4}$ . The cosine annealing strategy is utilized to adaptively reduce the learning rate to  $1.0 \times 10^{-6}$  during training. We used the Pytorch framework to implement our proposed model with two Nvidia 3090 GPUs, and the total number of epochs used in training is 300. It takes about two days to complete the training.

### B. Experiments on the Kalantari Dataset

In this experiment, our proposed model is denoted as MSANet. We compared MSANet with other state-of-the-art HDR methods, including Sen [36], DeepHDR [15], Wu [17], AHDRNet [13], PANet [25], and PSFNet [3]. We used the open-source code provided by the authors for testing, except for PANet. The code of PANet is not publicly available, so we directly refer to the results provided in the original paper. The average PSNR- $\mu$ , PSNR-L, SSIM- $\mu$ , SSIM-L, and HDR-VDP-2 of different HDR methods on the Kalantari dataset are tabulated in Table I. The best results are highlighted in bold. As observed, our proposed MSANet significantly outperforms all compared HDR methods in terms of all evaluation metrics. Compared with the second-best method (i.e., PSFNet), MASNet achieved 0.3dB and 1.3488 higher, in terms of the PSNR- $\mu$  and HDR-VDP-2, respectively. These results reveal that our method can generate high-quality HDR images in the tone-mapped and linear domains than other HDR methods. In addition, we selected two images from the Kalantari Dataset for visual comparison, and the results generated by different HDR methods are illustrated in Fig. 7. Two local regions marked by red and blue rectangles, which contain moving objects, are enlarged for better comparison. We can find that the results generated by DeepHDR, Wu, AHDRNet, and PSFNet contain undesirable ghosting artifacts and distorted contents in motion and overexposed regions. Although Sen can restore the corrupted content in saturated regions, it fails to handle motion regions and produces severe ghosting artifacts. These results show that the compared methods struggle to overcome object motions and compensate for corrupted content in saturated regions simultaneously. Compared with them, our method can effectively alleviate the ghosting artifacts caused by object motions and adequately compensate for the corrupted regions in under and overexposed regions. As a result, the HDR images generated by our method contain less distorted image content, leading to the best visual quality.

### C. Experiments on the Sen and Tursun Datasets

We further compare our proposed model with other HDR imaging methods in two challenging datasets, i.e., the Sen and Tursun datasets. Compared to the images in the Kalantari dataset, the LDR images in these two datasets were captured

at different exposure settings, and the reference images are relatively dark. This makes the reconstruction of HDR images more challenging. Therefore, we used these two datasets to evaluate the generalization ability of different HDR models. Since these two datasets do not provide ground-truth images for quantitative comparison, we compare the performance of different HDR methods through visual results. For each dataset, we selected one image for visual comparison. The images generated by different HDR imaging methods are illustrated in Fig. 8. For better comparison, two local regions marked by red and blue rectangles are cropped and then enlarged. As observed, the HDR images generated by Sen and DeepHDR are noisy and contain unpleasant artifacts caused by object motion. Although AHDRNet and PSFNet can produce satisfactory results in Fig. 8(a), severe ghosting artifacts can be easily observed in the underexposed regions which contain object motion, as shown in Fig. 8(b). In addition, PSFNet cannot preserve the shape of objects, so the generated images lose details. This means that AHDRNet and PSFNet are sensitive to exposure conditions and suffer from poor generalization. Compared with these HDR methods, our method can effectively reduce ghosting artifacts caused by object motion and has a better ability to preserve structural information in the generated HDR images. Therefore, HDR images generated by our proposed model are much cleaner with rich, detailed information and fewer distortions, and have the best perceptual quality.

### D. Model Analysis

1) *The effect of the number of sampled features*: Our method implicitly aligns the input LDR images in the feature space by sampling neighboring features around the misaligned pixels. Therefore, we conducted an experiment to investigate the effect of the number of sampled features on the performance. In this experiment, we evaluate the performance of our model with different numbers of sampled features in the Kalantari dataset. The number of sampling features  $N$  is set from 2 to 10. Fig. 9 shows the PSNR- $\mu$  of the models with different numbers of sampling features. As observed, the proposed model can achieve the best performance when the number of sampled features  $N$  is set to 3. When the number of sampled features is increased from 3 to 10, PSNR- $\mu$  decreases by 0.15dB, because some inaccurate sampled features are involved in the aggregation, which harms the performance.

2) *Modules in the Multi-scale Correspondence Alignment Sub-network*: The multi-scale correspondence alignment sub-network is a key component in our proposed model, which implicitly aligns LDR images in a coarse-to-fine manner. Therefore, we conducted an experiment to evaluate the performance of the alignment sub-network with different settings. Specifically, we will evaluate the performance of our proposed model with and without the use of the multi-scale structure. In addition, we will compare the performance of our model with different fusion methods across different scales, i.e., addition, concatenation, and the proposed inter-scale aggregation scheme. Other configurations of the models are the

TABLE I  
THE AVERAGE PSNR- $\mu$ , SSIM- $\mu$ , PSNR-L, SSIM-L, AND HDR-VDP-2 OF DIFFERENT METHODS ON THE KALANTARI DATASET. THE BEST RESULTS ARE HIGHLIGHTED IN BOLD.

Methods	Sen [36]	DeepHDR [15]	Wu [17]	AHDRNet [13]	PANet [25]	PSFNet [3]	MSANet (Ours)
PSNR- $\mu$	40.9689	42.7177	41.9977	43.7013	43.8487	44.0613	<b>44.3847</b>
PSNR-L	38.3425	41.2200	41.6593	41.1782	41.6452	41.5736	<b>42.1704</b>
SSIM- $\mu$	0.9859	0.9889	0.9878	0.9905	0.9906	0.9907	<b>0.9912</b>
SSIM-L	0.9764	0.9829	0.9860	0.9857	0.9870	0.9867	<b>0.9887</b>
HDR-VDP-2	60.3463	61.3139	61.7981	62.0521	62.5495	63.1550	<b>64.5038</b>

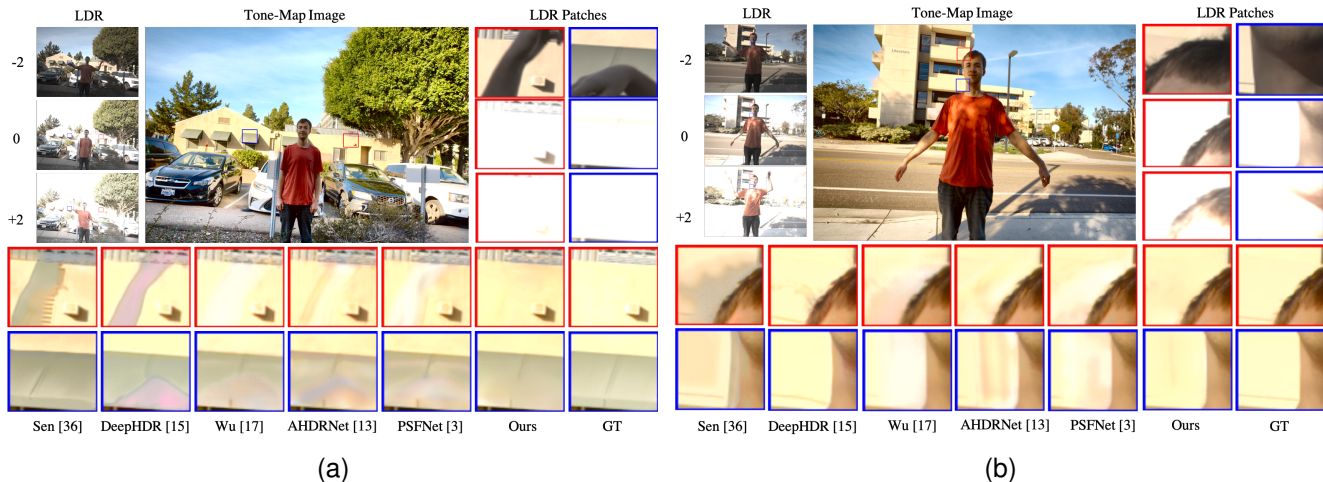


Fig. 7. Visual comparison of different HDR imaging methods. “-2”, “0”, and “+2” denote three different exposure settings. In the experiment, “0” represents the reference image.

same. The average PSNR- $\mu$ , SSIM- $\mu$ , and HDR-VDP-2 of our model with different settings on the Kalanrari dataset are shown in Table II. The best performance is highlighted in bold. As observed, the multi-scale structure with our proposed inter-scale aggregation scheme can significantly improve the performance by 0.55dB in terms of PSNR- $\mu$ . Compared with other fusion methods (i.e., addition and concatenation), the proposed inter-scale aggregation scheme achieves the best performance. This is because the proposed fusion scheme adaptively suppresses unnecessary pixels in the aggregation across scales. In addition, we show the images generated by our model with different settings in Fig. 10 for visual comparison. The models with the multi-scale structure have a better ability to generate images with rich, detailed information (e.g., tree branches) than that without the multi-scale structure. These results reveal that the multi-scale structure can effectively capture local details for better reconstruction. For the models using addition and concatenation fusions, the generated images suffer from color deviations. In contrast, our proposed inter-scale aggregation scheme can significantly reduce these distortions and produce images of better quality.

3) *Study on the Dense Wavelet Sub-network*: Our proposed dense wavelet sub-network is based on the DWT, which decomposes the input features into several non-overlapping frequency subbands for feature extraction and reconstruction. In addition, we utilize the group strategy and densely concatenate the outputs of the three Group WaveNets, so that

TABLE II  
THE AVERAGE PSNR- $\mu$ , SSIM- $\mu$ , AND HDR-VDP-2(VDP-2) OF OUR PROPOSED MODEL (MSANet) WITH DIFFERENT SETTINGS ON THE KALANRARI DATASET. “MS” REPRESENTS THE MULTI-SCALE STRUCTURE. “A”, “C”, AND “M” DENOTES THE ADDITION, CONCATENATION, AND OUR PROPOSED MASKING METHOD IN INTER-SCALE AGGREGATION. “✓” REPRESENTS THE CORRESPONDING METHOD USED IN MSANet. “✗” DENOTES THE MODEL WITHOUT USING THE METHOD.

Models	MS	Fusion			PSNR- $\mu$	SSIM- $\mu$	VDP-2
		A	C	M			
MSANet	✗	✗	✗	✗	44.0933	0.9910	63.6499
MSANet	✓	✓	✗	✗	44.2538	<b>0.9912</b>	64.3989
MSANet	✓	✗	✓	✗	44.1815	0.9911	64.1025
MSANet	✓	✗	✗	✓	<b>44.3847</b>	<b>0.9912</b>	<b>64.5038</b>

our method can fully utilize the information from intermediate layers. Therefore, we conduct an experiment to compare the performance of our method with and without the use of DWT. For the model without using DWT, it simply performs feature extraction over the spatial domain. Other configurations are the same as the model with DWT. Besides that, we also study the performance of our model using different numbers of groups. In our method, the total number of groups is six, so we set the number of groups  $G$  to 1, 2, and 3, respectively, in this experiment. The average PSNR- $\mu$ , SSIM- $\mu$ , and HDR-VDP-2



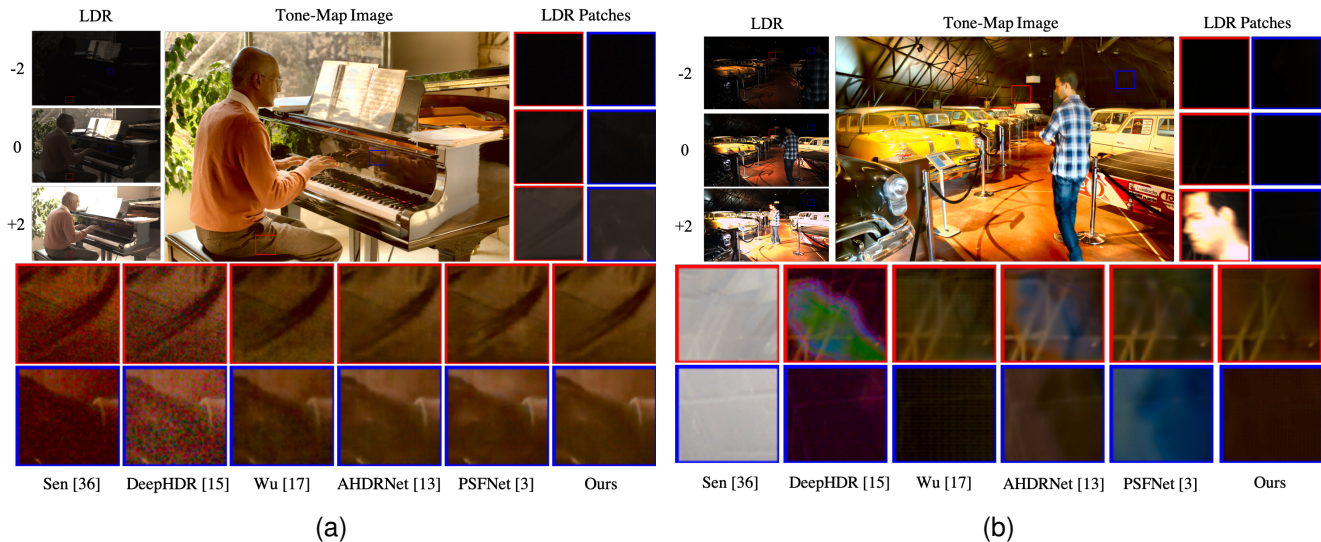


Fig. 8. Visual comparison of different HDR imaging methods. The image illustrated in (a) is selected from the Sen dataset, and the image shown in (b) is from the Tursun dataset.

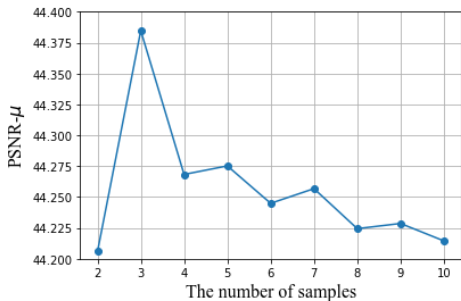


Fig. 9. The PSNR- $\mu$  of the model with different numbers of sampled features.

of our model with different settings on the Kalanrari dataset are tabulated in Table III. As observed, our model with DWT can achieve 0.13dB higher than the model without DWT in terms of PSNR- $\mu$ . This result shows that extracting features in the wavelet domain is more effective, because different frequency subbands provide different information for HDR image reconstruction. In addition, when the number of groups is increased, the performance of our model improves significantly, because having more groups can increase information interaction of different layers.

TABLE III  
THE AVERAGE PSNR- $\mu$ , SSIM- $\mu$ , AND HDR-VDP-2 OF THE MODELS WITH DIFFERENT SETTINGS ON THE KALANRARI DATASET. THE BEST RESULTS OF DIFFERENT SETTINGS ARE HIGHLIGHTED IN BOLD.

		PSNR- $\mu$	SSIM- $\mu$	HDR-VDP-2
Domain	w DWT	<b>44.3847</b>	<b>0.9912</b>	<b>64.5038</b>
	w/o DWT	44.1566	0.9910	64.0267
Group	$G = 1$	44.1203	0.9911	63.8058
	$G = 2$	44.2136	0.9910	64.3134
	$G = 3$	<b>44.3847</b>	<b>0.9912</b>	<b>64.5038</b>

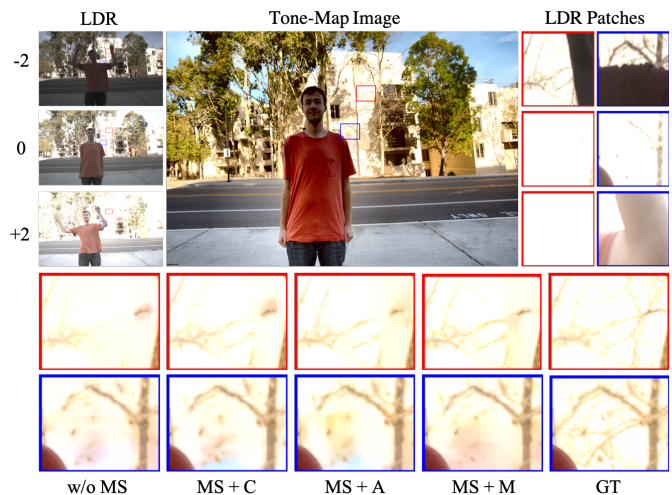


Fig. 10. The generated HDR images of our method (i.e., MASNet) with different settings. “w/o MS” represents the model without using the multi-scale structure. “MS+C”, “MS+A”, and “MS+M” represent that the model adopts concatenation, addition, and the proposed progressive masking method for fusion, respectively.

4) *Study on Different Types of Wavelets:* Our proposed HDR imaging method is based on DWT for HDR imaging, so we also investigate the performance of our model with different types of wavelets. Specifically, we compare the performance of our model with Haar wavelets, two symmetry wavelets, and two biorthogonal wavelets. These three wavelets have different properties. For example, Haar wavelets are asymmetric, but they are orthogonal and biorthogonal. In the experiment, the other configurations are the same. The average PSNR- $\mu$  and SSIM- $\mu$  of our model with different types of wavelets on the Kalanrari dataset are tabulated in Table IV. As observed, different wavelets used in our model will significantly affect the performance. The performances of the model with symmetry wavelets is lower than that with

Haar and biorthogonal wavelets. Compared with biorthogonal wavelets, the model with Haar wavelets can achieve slightly better performance because Haar wavelets are orthogonal. These results show that orthogonal and biorthogonal wavelets are more beneficial for reconstruction.

TABLE IV  
THE AVERAGE PSNR- $\mu$  AND SSIM- $\mu$  OF OUR MODEL WITH DIFFERENT WAVELETS ON THE KALANRARI DATASET. THE BEST RESULTS ARE HIGHLIGHTED IN BOLD.

	Haar	Symmetry		Biorthogonal	
		sym2	sym5	bio1.1	bio3.5
PSNR- $\mu$	<b>44.38</b>	44.29	44.08	44.35	44.18
SSIM- $\mu$	0.9912	<b>0.9913</b>	0.9911	0.9912	0.9912

## V. CONCLUSION

High dynamic range (HDR) imaging in dynamic scenes is still a challenging problem. Most existing HDR methods produce results with undesirable ghosting artifacts caused by misalignment between low dynamic range (LDR) images. In addition, adequate compensation should also be applied to the corrupted contents in under and overexposed regions. Otherwise, distortions will appear in the generated HDR images. In this paper, we propose a multi-scale sampling and aggregation network for HDR imaging in dynamic scenes. The proposed method implicitly aligns LDR images by sampling and aggregating high-correspondence features around the misaligned pixels at different scale spaces. Then, the aggregated features are progressively fused in a coarse-to-fine manner, so our proposed method can effectively reduce the ghosting artifacts caused by object motion. In addition, we propose a dense wavelet sub-network to merge the aligned features and generate corresponding HDR images, which decomposes the input into several non-overlap frequency subbands for feature extraction. Different frequency subbands contain different information for reconstruction, so our method can effectively compensate for corrupted content in saturated regions. Experiments show that our proposed model significantly outperforms other HDR methods and achieves the best results. In addition, the HDR images generated by our model contain fewer distortions and more detailed content, leading to the best visual quality.

## REFERENCES

- [1] J. Froehlich, S. Grandinetti, B. Eberhardt, S. Walter, A. Schilling, and H. Brendel, "Creating cinematic wide gamut hdr-video for the evaluation of tone mapping operators and hdr-displays," in *Digital photography X*, vol. 9023. International Society for Optics and Photonics, 2014, p. 90230X.
- [2] M. D. Tocci, C. Kiser, N. Tocci, and P. Sen, "A versatile hdr video production system," *ACM Transactions on Graphics (TOG)*, vol. 30, no. 4, pp. 1–10, 2011.
- [3] Q. Ye, J. Xiao, K.-M. Lam, and T. Okatani, "Progressive and selective fusion network for high dynamic range

- imaging," in *Proceedings of the 29th ACM International Conference on Multimedia*, 2021, pp. 5290–5297.
- [4] L. Bogoni, "Extending dynamic range of monochrome and color images through fusion," in *Proceedings of the International Conference on Pattern Recognition.*, vol. 3. IEEE, 2000, pp. 7–12.
- [5] E. A. Khan, A. O. Akyuz, and E. Reinhard, "Ghost removal in high dynamic range images," in *Proceedings of the International Conference on Image Processing*. IEEE, 2006, pp. 2005–2008.
- [6] K. Jacobs, C. Loscos, and G. Ward, "Automatic high-dynamic range image generation for dynamic scenes," *IEEE Computer Graphics and Applications*, vol. 28, no. 2, pp. 84–93, 2008.
- [7] E. Reinhard, W. Heidrich, P. Debevec, S. Pattanaik, G. Ward, and K. Myszkowski, *High dynamic range imaging: acquisition, display, and image-based lighting*. Morgan Kaufmann, 2010.
- [8] O. Gallo, N. Gelfandz, W.-C. Chen, M. Tico, and K. Pulli, "Artifact-free high dynamic range imaging," in *2009 IEEE International conference on computational photography (ICCP)*. IEEE, 2009, pp. 1–7.
- [9] T. Grosch, "Fast and robust high dynamic range image generation with camera and object movement," *Vision, Modeling and Visualization, RWTH Aachen*, pp. 277–284, 2006.
- [10] T.-H. Oh, J.-Y. Lee, Y.-W. Tai, and I. S. Kweon, "Robust high dynamic range imaging by rank minimization," *IEEE Transactions on Pattern Analysis and Machine Intelligence*, vol. 37, no. 6, pp. 1219–1232, 2014.
- [11] Q. Yan, J. Sun, H. Li, Y. Zhu, and Y. Zhang, "High dynamic range imaging by sparse representation," *Neurocomputing*, vol. 269, pp. 160–169, 2017.
- [12] C. Lee, Y. Li, and V. Monga, "Ghost-free high dynamic range imaging via rank minimization," *IEEE Signal Processing Letters*, vol. 21, no. 9, pp. 1045–1049, 2014.
- [13] Q. Yan, D. Gong, Q. Shi, A. v. d. Hengel, C. Shen, I. Reid, and Y. Zhang, "Attention-guided network for ghost-free high dynamic range imaging," in *Proceedings of the IEEE/CVF Conference on Computer Vision and Pattern Recognition*, 2019, pp. 1751–1760.
- [14] Q. Yan, Y. Zhu, and Y. Zhang, "Robust artifact-free high dynamic range imaging of dynamic scenes," *Multimedia Tools and Applications*, vol. 78, no. 9, pp. 11 487–11 505, 2019.
- [15] N. K. Kalantari, R. Ramamoorthi *et al.*, "Deep high dynamic range imaging of dynamic scenes," *ACM Transactions on Graphics (TOG)*, vol. 36, no. 4, pp. 144–1, 2017.
- [16] D. Hafner, O. Demetz, and J. Weickert, "Simultaneous hdr and optic flow computation," in *Proceedings of the International Conference on Pattern Recognition*. IEEE, 2014, pp. 2065–2070.
- [17] S. Wu, J. Xu, Y.-W. Tai, and C.-K. Tang, "Deep high dynamic range imaging with large foreground motions," in *Proceedings of the European Conference on Computer Vision (ECCV)*, 2018, pp. 117–132.
- [18] W. Zhang and W.-K. Cham, "Gradient-directed mul-

- tiexposure composition,” *IEEE Transactions on Image Processing*, vol. 21, no. 4, pp. 2318–2323, 2011.
- [19] S.-h. Lee, J. S. Park, and N. I. Cho, “A multi-exposure image fusion based on the adaptive weights reflecting the relative pixel intensity and global gradient,” in *Proceedings of the IEEE International Conference on Image Processing (ICIP)*. IEEE, 2018, pp. 1737–1741.
- [20] C. Liu *et al.*, “Beyond pixels: exploring new representations and applications for motion analysis,” Ph.D. dissertation, Massachusetts Institute of Technology, 2009.
- [21] D. Sun, X. Yang, M.-Y. Liu, and J. Kautz, “Pwc-net: Cnns for optical flow using pyramid, warping, and cost volume,” in *Proceedings of the IEEE Conference on Computer Vision and Pattern Recognition (CVPR)*, 2018, pp. 8934–8943.
- [22] J. J. Yu, A. W. Harley, and K. G. Derpanis, “Back to basics: Unsupervised learning of optical flow via brightness constancy and motion smoothness,” in *Proceedings of the European Conference on Computer Vision (ECCV)*. Springer, 2016, pp. 3–10.
- [23] Z. Teed and J. Deng, “Raft: Recurrent all-pairs field transforms for optical flow,” in *Proceedings of the European Conference on Computer Vision*. Springer, 2020, pp. 402–419.
- [24] X. Zhu, H. Hu, S. Lin, and J. Dai, “Deformable convnets v2: More deformable, better results,” in *Proceedings of the IEEE/CVF Conference on Computer Vision and Pattern Recognition*, 2019, pp. 9308–9316.
- [25] Z. Pu, P. Guo, M. S. Asif, and Z. Ma, “Robust high dynamic range (hdr) imaging with complex motion and parallax,” in *Proceedings of the Asian Conference on Computer Vision*, 2020.
- [26] X. Wang, K. C. Chan, K. Yu, C. Dong, and C. Change Loy, “Edvr: Video restoration with enhanced deformable convolutional networks,” in *Proceedings of the IEEE/CVF Conference on Computer Vision and Pattern Recognition Workshops*, 2019, pp. 0–0.
- [27] Z. Liu, W. Lin, X. Li, Q. Rao, T. Jiang, M. Han, H. Fan, J. Sun, and S. Liu, “Adnet: Attention-guided deformable convolutional network for high dynamic range imaging,” in *Proceedings of the IEEE/CVF Conference on Computer Vision and Pattern Recognition Workshop*, 2021, pp. 463–470.
- [28] K. C. Chan, X. Wang, K. Yu, C. Dong, and C. C. Loy, “Understanding deformable alignment in video super-resolution,” in *Proceedings of the AAAI Conference on Artificial Intelligence*, vol. 35, no. 2, 2021, pp. 973–981.
- [29] S. Raman and S. Chaudhuri, “Reconstruction of high contrast images for dynamic scenes,” *The Visual Computer*, vol. 27, no. 12, pp. 1099–1114, 2011.
- [30] Y. S. Heo, K. M. Lee, S. U. Lee, Y. Moon, and J. Cha, “Ghost-free high dynamic range imaging,” in *Proceedings of the Asian Conference on Computer Vision*. Springer, 2010, pp. 486–500.
- [31] A. Tomaszewska and R. Mantiuk, “Image registration for multi-exposure high dynamic range image acquisition,” 2007.
- [32] T. Mitsunaga and S. K. Nayar, “Radiometric self calibration,” in *Proceedings. 1999 IEEE computer society conference on computer vision and pattern recognition (Cat. No PR00149)*, vol. 1. IEEE, 1999, pp. 374–380.
- [33] H. Zimmer, A. Bruhn, and J. Weickert, “Freehand hdr imaging of moving scenes with simultaneous resolution enhancement,” in *Computer Graphics Forum*, vol. 30, no. 2. Wiley Online Library, 2011, pp. 405–414.
- [34] J. Hu, O. Gallo, K. Pulli, and X. Sun, “Hdr deghosting: How to deal with saturation?” in *Proceedings of the IEEE/CVF Conference on Computer Vision and Pattern Recognition*, 2013, pp. 1163–1170.
- [35] S. B. Kang, M. Uyttendaele, S. Winder, and R. Szeliski, “High dynamic range video,” *ACM Transactions on Graphics (TOG)*, vol. 22, no. 3, pp. 319–325, 2003.
- [36] P. Sen, N. K. Kalantari, M. Yaesoubi, S. Darabi, D. B. Goldman, and E. Shechtman, “Robust patch-based hdr reconstruction of dynamic scenes,” *ACM Transactions on Graphics (TOG)*, vol. 31, no. 6, pp. 203–1, 2012.
- [37] Q. Yan, L. Zhang, Y. Liu, Y. Zhu, J. Sun, Q. Shi, and Y. Zhang, “Deep hdr imaging via a non-local network,” *IEEE Transactions on Image Processing*, vol. 29, pp. 4308–4322, 2020.
- [38] J. Chen, Z. Yang, T. N. Chan, H. Li, J. Hou, and L.-P. Chau, “Attention-guided progressive neural texture fusion for high dynamic range image restoration,” *IEEE Transactions on Image Processing*, vol. 31, pp. 2661–2672, 2022.
- [39] Y. Niu, J. Wu, W. Liu, W. Guo, and R. W. Lau, “Hdrgan: Hdr image reconstruction from multi-exposed ldr images with large motions,” *IEEE Transactions on Image Processing*, vol. 30, pp. 3885–3896, 2021.
- [40] X. Mao, Q. Li, H. Xie, R. Y. Lau, Z. Wang, and S. Paul Smolley, “Least squares generative adversarial networks,” in *Proceedings of the IEEE International Conference on Computer Vision*, 2017, pp. 2794–2802.
- [41] J. Adler and S. Lunz, “Banach wasserstein gan,” *Proceedings of the Advances in Neural Information Processing Systems*, vol. 31, 2018.
- [42] I. Gulrajani, F. Ahmed, M. Arjovsky, V. Dumoulin, and A. C. Courville, “Improved training of wasserstein gans,” *Proceedings of the Advances in neural information processing systems*, vol. 30, 2017.
- [43] J. Hu, L. Shen, and G. Sun, “Squeeze-and-excitation networks,” in *Proceedings of the IEEE Conference on Computer Vision and Pattern Recognition*, 2018, pp. 7132–7141.
- [44] O. T. Tursun, A. O. Akyüz, A. Erdem, and E. Erdem, “An objective deghosting quality metric for hdr images,” in *Computer Graphics Forum*, vol. 35, no. 2. Wiley Online Library, 2016, pp. 139–152.
- [45] R. Mantiuk, K. J. Kim, A. G. Rempel, and W. Heidrich, “Hdr-vdp-2: A calibrated visual metric for visibility and quality predictions in all luminance conditions,” *ACM Transactions on graphics (TOG)*, vol. 30, no. 4, pp. 1–14, 2011.